Optical design of a compact imaging spectrometer for planetary mineralogy

Pantazis Mouroulis, FELLOW SPIE
R. Glenn Sellar, MEMBER SPIE
Daniel W. Wilson
Jet Propulsion Laboratory
California Institute of Technology
Pasadena, California 91109
E-mail: Pantazis.mouroulis@jpl.nasa.gov

James J. Shea
Alliant Techsystems (ATK)
404 North Halstead Street
Pasadena, California 91107

Robert O. Green
Jet Propulsion Laboratory
California Institute of Technology
Pasadena, California 91109

Abstract. We present the design of a compact, wide-angle pushbroom imaging spectrometer suitable for exploration of solar system bodies from low orbit. The spectrometer is based on a single detector array with a broadband response that covers the range 400 to 3000 nm and provides a spectral sampling of 10 nm. The telescope has a 24-deg field of view with 600 spatially resolved elements (detector pixels). A specially designed convex diffraction grating permits optimization of the signal-to-noise ratio through the entire spectral band. Tolerances and design parameters permit the achievement of high uniformity of response through field and wavelength. The spectrometer performance is evaluated in terms of predicted spectral and spatial response functions and from the point of view of minimizing their variation through field and wavelength. The design serves as an example for illustrating the design principles specific to this type of system. [DOI: 10.1117/1.2749499]

Subject terms: spectrometers; optical design; space optics; imaging spectroscopy.

Paper 060664R received Aug. 23, 2006; revised manuscript received Dec. 5, 2006; accepted for publication Dec. 21, 2006; published online Jun. 29, 2007.

1 Introduction

Imaging spectrometers are ideal for identifying minerals and mapping their distribution utilizing solar reflected illumination. This has been shown with investigations of the Earth from either aircraft[1,2] or satellite.[3] Pioneering work has been done with the airborne whiskbroom sensor Airborne Visible/Infrared Imaging Spectrometer (AVIRIS)[2] which is still in operation. Hyperion, a pushbroom sensor, has been the first Earth-orbiting spectrometer to routinely acquire science-grade data.[3]

In addition to Hyperion, planetary imaging spectrometers include the Visual and Infrared Mapping Spectrometer (VIMS) instrument[4] on board the Cassini spacecraft now orbiting the Saturnian system, and the CRISM instrument[5] now orbiting Mars. VIMS comprises two separate instruments, a pushbroom and a whiskbroom scanner, covering the 0.3 to 1 and 1 to 5-μm range, respectively. The Compact Reconnaissance Imaging Spectrometer for Mars (CRISM) has a common telescope for two separate Offner-type spectrometers, covering a similar range, while Hyperion also has a similar dual spectrometer design with the spectral range limited to 2.5-μm. The present design integrates both spectrometers into a single, miniature instrument that offers the same or greater number of spatially resolved channels, covering the spectral range 0.4 to 3 μm with a similar spectral resolution, in addition to improving by up to a factor of 4 the uniformity of response.

The design specifications are guided by the requirements of the Moon Mineralogy Mapper (M3) instrument, which is a pushbroom imaging spectrometer built by the Jet Propulsion Laboratory and scheduled for launch aboard the Indian Space Research Organization's Chandrayaan-1 lunar orbiting spacecraft. The scientific goal of the investigation is to obtain accurate reflectance spectral image cubes from 430 to 3000 nm at a spatial sampling of $\sim$70 m and spectral sampling of $\sim$10 nm for $>$ 5% of the lunar surface as targeted scenes ($\sim 40 \times 40$ km) with high signal to noise ratios (at least 400 and 100 at the equatorial and polar reference radiances). Mission-specific information and a general description of that instrument can be found in Ref. 6. However, although specific requirements are needed to complete any optical design, the design itself as well as the principles, procedures, and recommendations described here are of more general validity.

Although there are now several pushbroom imaging spectrometers in operation or in planning, the design principles have not been clearly articulated in the literature. The achievement of uniformity of response (spectral response independent of field and spatial response independent of wavelength) is paramount in this type of spectrometer.[7] In addition to presenting a specific, advanced design, this work aims to demonstrate the principles of design and evaluation of a complete pushbroom imaging spectrometer system that can lead to the achievement of high response uniformity.

2 System Specification

The system spatial, spectral, and radiometric specifications are described in Tables 1 and 2. The following acronyms are used: spectral response function (SRF), field of view (FOV), full-width at half-maximum (FWHM), cross-track spatial response function (CRF), along-track spatial response function (ARF), signal-to-noise ratio (SNR), and focal plane array (FPA). Only those specifications that are relevant to the aims of this work are shown.

0091-3286/2007/$25.00

Table 1 First-order specifications. The SNR is meaningful only at a given reference radiance, provided by the application.

Full FOV	24 deg
Cross-track spatial samples	600
Number of spectral channels	260
Spectral range	400 to 3000 nm
Spectral sampling	10 nm
Mass (optics bench)	1.5 kg
FPA pixel size	27 μm
SNR	≥400

It is to be noted that these specifications in combination have never before been reached in a space-qualified system. The design presented here achieves this performance while simultaneously providing significant mass reduction over the state of the art.

3 Optical Design Description and Procedure

A complete system ray trace is shown in Fig. 1. The system comprises a three-mirror anastigmat (TMA) telescope and an Offner-type spectrometer, with a slit placed at the telescope focus. The focal plane array (FPA), which is commercially available, can handle the entire spectral range and in turn enables the use of a single spectrometer and a grating operating in a single order.

Table 2 Resolution and response uniformity specifications. The design column are values achieved by the as-toleranced design, after fabrication, assembly, and launch tolerances have been accounted for.

Specification	Goal	Design
SRF FWHM all fields and wavelengths	<15 nm	14.7 nm
CRF FWHM all fields and wavelengths	<1.5 sample	1.13 sample
ARF FWHM all fields and wavelengths	<1.5 sample	1.20 sample
CRF center variation with wavelength (keystone)	<0.1 pixel	0.07 pixel
CRF FWHM variation with wavelength	<0.15 pixel	0.04 pixel
ARF FWHM variation with wavelength	<0.15 pixel	0.10 pixel
SRF center variation with field (smile or frown)	<0.1 pixel	0.08 pixel
SRF FWHM variation with field	<0.1 pixel	0.10 pixel

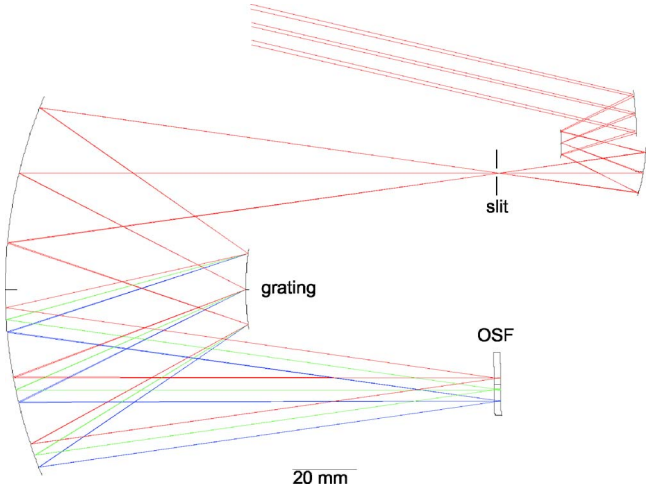

Fig. 1 Complete system raytrace. OSF stands for order-sorting filter.

3.1 *Telescope Design*

The TMA design is of minimum size and very nearly telecentric in the image space, thus providing a good pupil match with the spectrometer design. It comprises three conical surfaces with a common axis of rotational symmetry. Minimization of wavefront error is the only criterion used in optimizing the telescope. The resulting design is nearly diffraction limited through the entire field. The specifications and performance are given in Table 3.

The last line of this table deserves a short explanation. Specifically, no attempt is made to project a straight slit image on the ground, since in any case the curvature and irregularity of the ground make the concept meaningless. This line curvature (or distortion) produced by the telescope can be calibrated accurately, is not sensitive to tolerances, and can be corrected through tried image rectification techniques.

An important design principle is to oversize the telescope aperture to allow the system aperture stop to be located at the grating without vignetting anywhere else in the system. Thus the f number of the telescope in isolation is 3.15, but the geometric working f number of 3.55 is determined by the spectrometer. The oversizing of the telescope aperture has a small but measurable effect on performance, as is explained later. Telescope spot diagrams are shown in Fig. 2.

Table 3 Telescope specifications and performance.

Focal length	40.18 mm
Working *F*/number	3.55
Exit pupil position (paraxial)	–2600 mm
FOV (*x* direction)	±12 deg
Geometric spot size (rms)	<2.1 μm for all field positions
Curvature of slit image (*y* direction)	0.31 deg

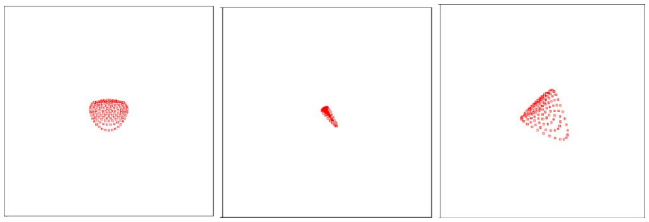

Fig. 2 Telescope spot diagrams shown in a 27-μm square box. From left to right: middle of the field, 9 deg, and 12 deg (top end of the slit). The other half of the FOV gives symmetrical results.

3.2 *Spectrometer Design*

The spectrometer is of the Offner type,[8] with a single spherical mirror acting as primary and tertiary, and a spherical (convex) diffraction grating. The first-order parameters are described in Table 4. The large spectral range necessitates the use of a segmented order-sorting filter, placed in close proximity to the FPA. The filter has negligible impact on optical performance and is not discussed further.

The spectrometer spot diagrams are shown in Fig. 3. Although they are not a good way of assessing the system performance, they give an idea of the level of aberration in the system. The system performance is assessed in a more suitable way in Sec. 5. It is noted that the short-wavelength spots are intentionally degraded in the spatial (x) direction to balance the increased diffraction from the long wavelength and thus improve the CRF uniformity. The variation observed along the y direction as a function of field is inevitable for this simple design, which does not possess enough degrees of freedom to achieve uniformity levels of 1 to 2%, even though the design was optimized according to the principles of Ref. 7. Better design performance is possible by separating primary and tertiary,[9] but simplicity of construction and alignment results from the use of a single mirror. In any case, even this simple design satisfies the stringent specifications of Tables 1 and 2, as is shown next.

3.3 *Grating Design*

The grating design is an integral part of the optical design, not only in terms of the geometric parameters, but also in terms of its diffractive properties. The grating is required to cover in a single order a wider band than is possible with a traditional blazed design. Electron-beam lithography has been shown to be advantageous in producing gratings with various groove profiles and partitions.[10,11] The flexibility of the technique allows us to tailor the grating efficiency in such a way as to optimize the spectral dependence of the signal-to-noise ratio (SNR).

One solution to providing a broad-band response that has been previously demonstrated and implemented is to separate the grating into different areas, each of which has a different blaze angle. It is normally advantageous if the areas are annular zones. Three different zones would be required to produce the desired grating efficiency profile of Fig. 4. However, the three zones have very different individual responses, producing significant wavelength-dependent apodization and dephasing effects, which must

Table 4 Spectrometer first-order parameters.

Magnification	−1.00
F/number	3.55
Slit dimensions (FOV)	16.2 mm × 27 μm
Entrance pupil position (paraxial)	2900 mm
Exit pupil position (paraxial)	3046 mm
Grating period	29.184 μm
Grating operating order	−1

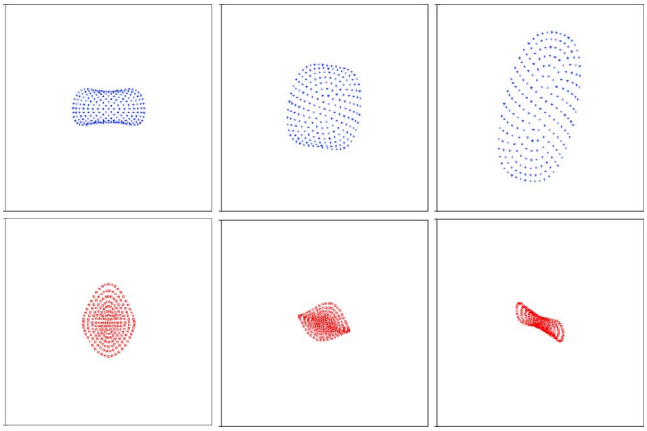

Fig. 3 Spectrometer-only spot diagrams for 400 nm (top) and 3000 nm wavelength (bottom). The box is the size of one detector pixel (27 μm). The middle of the field (slit) is on the left and the edge of the slit on the right, with an intermediate point in the middle. Diagrams for the other half of the slit are mirror images of those before. The spectral direction is along the vertical (y).

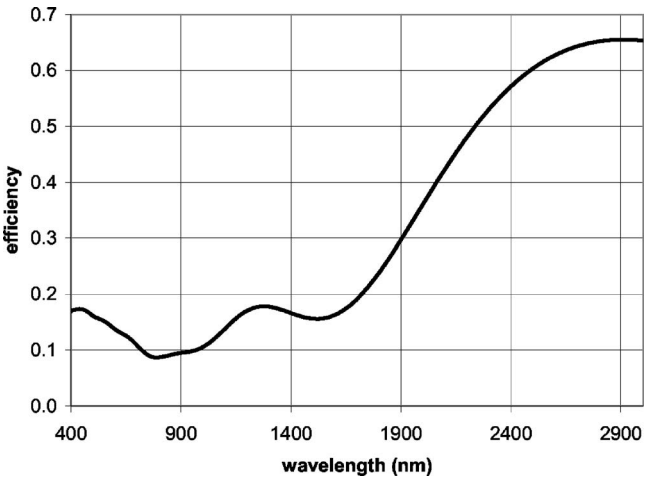

Fig. 4 Desired grating efficiency through wavelength, based on three partitions with different blaze angles. The curve emphasizes the long wavelengths where the solar spectrum is weak, as well as giving a small extra boost to the very short wavelengths to balance the detector response.

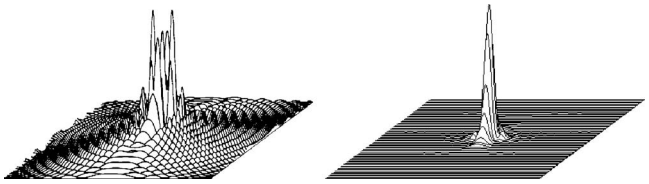

Fig. 5 PSF obtained by properly accounting for grating apodization and dephasing effects in a three-blaze design (left), and the corresponding PSF obtained by treating the grating as uniform (right). The box size is 2×2 pixels. The corresponding ensquared energy in a single 27-μm pixel is 44 and 97%.

be accounted for in deriving the PSF and hence the spectral and spatial responses. All these effects must be modeled in detail or the designer may underestimate dramatically the effect of the grating on the PSF. This is illustrated in Fig. 5, where we show the PSF obtained by neglecting apodization and dephasing effects and compared it with the actual expected PSF. In this case, if the designer were to treat the grating as uniform, a falsely near-perfect PSF would result. However, the real PSF would show substantial degradation that would have a considerable effect on the system performance. Raytracing and diffraction computations have been performed with ZEMAX (Focus Software, Bellevue, WA).

Several alternative partitioning and blazing schemes were examined. However, when the PSF variation was translated into response nonuniformity, it was determined that even in the best case, a multiple-area blazed grating would leave a residual CRF nonuniformity of more than 15%, thus not meeting the uniformity target.

The chosen solution was to modify the groove profile but maintain the same profile across the entire face of the grating. This removes all apodization and dephasing effects. A simple, bilinear groove profile suffices to approximate the desired response quite closely. This is an optimized version of the profile presented in Fig. 13 of Ref. 11. The resulting response is shown in Fig. 6, calculated using PCGrate software (Internatron Intellectual Group, Penfield, New York).

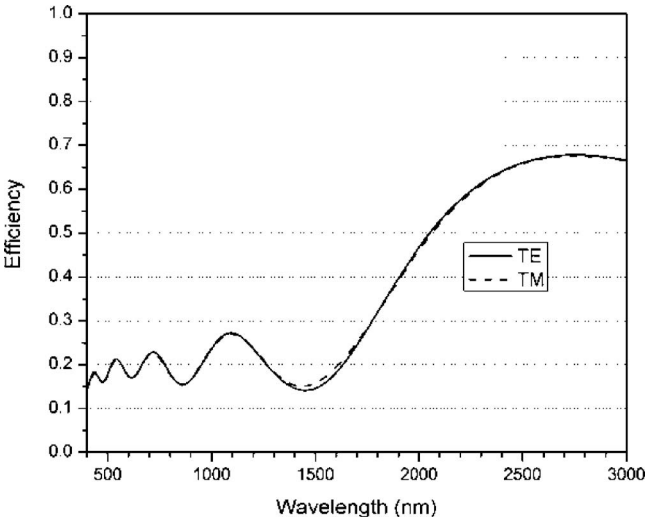

Fig. 6 First-order diffraction efficiency of a bilinear groove grating, adjusted for optimum SNR.

3.4 *System Integration*

The optical design procedure involves optimizing telescope and spectrometer in isolation, according to different optimization criteria. Suitable optimization criteria for the spectrometer have been discussed in detail.[7] The telescope is simply optimized for minimum wavefront error. The only connection between the two separate designs is the condition for pupil matching, so that the exit pupil of the telescope is approximately coincident with the entrance pupil of the spectrometer. With that condition satisfied, the two optimized designs are merely concatenated and the system aperture stop is set at the grating. No further optimization of the entire system is performed nor is it necessary. In fact, reoptimization of the complete system may produce the opposite of the intended result by destroying the spectral uniformity achieved during spectrometer optimization if the telescope is made to balance the aberrations of the spectrometer. A reoptimization that treats the whole system as a single unit while ignoring diffraction from the slit is based on physically incorrect assumptions. Of the three response functions of interest (SRF, CRF, and ARF), only the CRF involves the complete system PSF and is mostly (but not totally) unaffected by the slit. Thus a reoptimization of the complete system effectively optimizes the CRF only, while ignoring the other two responses.

When the two subsystems have been put together in the software, the field angle of the telescope along the y axis is then adjusted so that all telescope field points form a perfectly straight line image representing the slit. Conversely, the slit image on the ground ends up slightly curved, but this effect can be corrected by image rectification techniques, as explained in Sec. 3.1.

4 Tolerancing

A tolerancing approach for high-uniformity imaging spectrometers has been previously developed.[12] The approach, however, concerned only the spectrometer portion. Also, the particular system example achieved a broadband response by splitting the spectrum between two different spectrometer modules. As a result, it was found that the magnification difference between the two modules dominated the response nonuniformity. Thanks to the single spectrometer design, the present system achieves the same performance but with looser tolerances, such that can be satisfied with careful but not too difficult machining or particularly demanding optical shop practices.

The tolerancing procedure is as follows. First, the spectrometer and telescope are toleranced as separate units, using the merit functions developed for each. For the telescope, the back focus is used as compensator. For the spectrometer, the compensators are the back focus as well as the three angular degrees of freedom that represent focal plane adjustments during assembly. Once an acceptable level of individual errors has been determined, Monte Carlo simulations of each subsystem are produced, in which the errors are distributed randomly according to a uniform distribution. We then select sample perturbed telescope and spectrometer realizations that are distributed around the 90th percentile, and pair them to produce complete systems. In doing so, the y field values of the perturbed telescopes must be readjusted by hand to represent a straight

slit. These sample systems are then subjected to a second set of perturbations, of much smaller magnitude than the first set, which represent vibration and thermal effects of the complete system after launch. No compensators are used during this phase, since none are available in practice. A second set of 90th percentile samples is then selected and the performance metrics calculated. These represent the on-orbit estimate of performance.

The summary tolerance allocations are shown in Table 5. A value of 0 is entered when the corresponding number is less than 0.005, and all entries are rounded to 0.01. The slit allocation represents slit imperfections (deviation from straightness and width nonuniformity) that are not inherent to the design. The totals represent the sum of all factors as an appropriately pessimistic estimate. It may be seen that all design goals are met, assuming a 0.01 SRF nonuniformity allocation from the slit, which can be achieved with a high quality, lithographically manufactured slit.

5 Performance Measures and System Assessment

Imaging spectrometers cannot be assessed adequately through typical lens design figures of merit such as spot size or MTF. Uniformity of response is normally more important than minimization of wavefront error. We show in this section a way of assessing and computing the instrument performance that utilizes those performance metrics that are of importance to the final user. We also demonstrate that accurate assessment of the performance involves detailed diffraction propagation computation through the entire system that accounts for diffraction at the slit and cannot be performed through simple raytracing. Performance figures derived from raytracing are adequate at the short wavelength end, where diffraction from the slit is negligible.

5.1 *Radiometric and Signal-to-Noise Ratio Assessment*

The SNR is estimated through the target radiance, optical system aperture and transmittance, photodetector response, photon, electronic and thermal noise, and scattered radiance. The detailed computation of the SNR is outside the scope of this work, since the SNR goals are specific to the target and the scientific investigation. We concentrate here only on two aspects of importance, specifically the effects of the grating response and of slit diffraction.

The grating spectral response of Fig. 6 has the effect of flattening the SNR curve through wavelength. The prediction is shown in Fig. 7. It can be seen that the SNR is maintained at a good value everywhere, despite the strong variation of the solar spectrum over this range. Of particular note is the high SNR at the long wavelength end, a direct result of the high grating efficiency over the corresponding range (Fig. 6).

The computation of SNR also accounts for light diffracted at the slit outside the spectrometer aperture. This results in a wavelength-dependent transmission correction factor, shown in Fig. 8. When the telescope aperture is oversized, this loss factor is minimized. If the telescope is sized to the same aperture as the spectrometer, the resulting light loss is $\sim$ 18% at the long wavelength end,[13] in addition to any vignetting losses due to pupil mismatch. The actual loss factor is computed through detailed diffraction computation through the system apertures and slit.

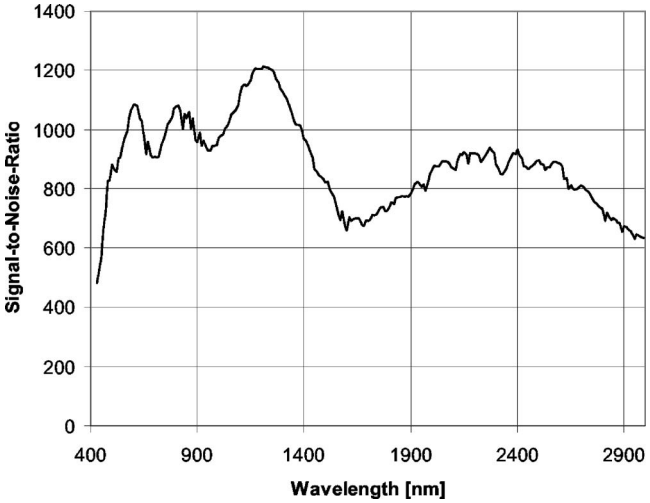

Fig. 7 SNR through wavelength.

5.2 *Assessment of Spectral Response Function and Spectral Uniformity*

Three computations are required for this assessment: 1. the SRF FWHM value through field and wavelength, which is a measure of the spectral resolution; 2. the SRF FWHM variation through field for any given wavelength; and 3. the spectral distortion ("smile"), representing the SRF centroid location.

Starting with the simplest one first, smile is assessed through the geometrical spot centroid location for any wavelength as a function of field, which is known to coincide with the diffraction centroid.[14] This is achieved through a simple raytrace of the spectrometer alone; the telescope has no effect on this, even if its aberrations vary through field (assuming a uniform object of extent greater

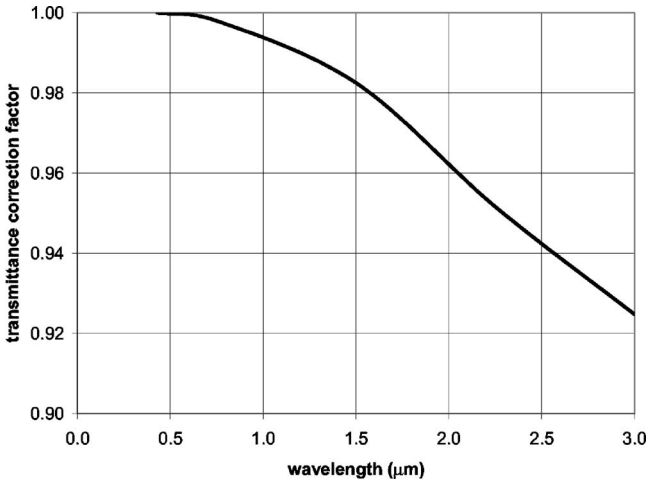

Fig. 8 Radiometric correction factor for 13% oversized (by diameter) telescope pupil.

Table 5 Tolerance allocations.

	Resolution			Distortion		Response uniformity		
	Spectral	Along track	Cross track	SRF center	CRF center	SRF width	CRF width	ARF width
Design	1.41	1.12	1.06	0	0	0.06	0.01	0.07
Tol. 1	0.02	0.02	0.02	0.06	0.07	0.02	0.02	0.02
Tol. 2	0.04	0.04	0.05	0.01	0	0.01	0.01	0.01
Slit				0.01		0.01		
Total	1.47	1.18	1.13	0.08	0.07	0.10	0.04	0.10

than the spatial resolution of the system). For the design presented here, the residual value is negligible ($\sim$0.001 pixel), as Table 5 shows.

The other two computations involve Fresnel diffraction propagation, starting with an oversized plane wave presented to the telescope. This is propagated first through the telescope, allowing the various mirror apertures to vignette the beam, though in practice only the local aperture stop size (telescope secondary) has a visible effect, allowing the telescope to be simplified and saving computation time. The plane wave will focus on the slit plane, and depending on its object-space angle, will be more or less obstructed by the slit. The slit thickness (if formed on metal foil) may also need to be considered, since any waveguiding effect will tend to produce a narrower response. The truncated complex amplitude distribution emerging from the slit is further propagated through the spectrometer to the FPA. The computation is then repeated for a small range of angles spanning the slit width, with each spot showing progressively more vignetting by the slit up to the point where the spot is completely obstructed (or less than 1% of the spot energy passes through). The sum of all the resulting intensity distributions at the focal plane gives an effective PSF that accounts for diffraction throughout the system; integration along the slit (spatial) direction then yields the equivalent line spread function (ELSF), which represents the monochromatic image of the slit as seen at the detector. At the long wavelength end, this can be significantly different from the image that would be computed through convolution of the slit width with the system PSF. In the absence of spectrometer aberrations or defocus, the ELSF is generally narrower than the slit.[13] At the short wavelength end, the effects of slit diffraction become negligible and the system performance can be approximated sufficiently without involving the long Fresnel diffraction computation.

The spectral response function is then computed by the convolution of the ELSF with the detector pixel response function, as well as a function representing the effect of the finite number of grating rulings. Theoretical simulations suggest that the detector response can be approximated by a Gaussian function, at least at the long wavelength end, and that the response broadens toward the shorter wavelengths. We have assumed a FWHM of 0.88 pixel units at 3000 nm, increasing by 10% toward the short wavelength end. However, the accuracy of these theoretical predictions is not at issue here. In practice, it would be necessary to obtain experimental detector response through wavelength, and then account for the actual measured function as well as its chromatic variation. For the purposes of this work, it suffices to show that a typical detector response and variation can be accommodated within the system specifications.

Figure 9 compares the predicted SRF at 3000 nm in the incoherent approximation, which neglects diffraction at the slit, and the actual expected response computed through detailed diffraction propagation. A difference of 7% in FWHM is seen. The difference between these two curves would have been greater ($\sim$11%) if the telescope aperture had not been oversized.

The maximum variation of SRF width with field occurs at the short wavelength end, as can also be surmised by the spot diagrams of Fig. 3. Nonetheless, since the spots are well contained within the pixel, the variation is not large. Figure 10 shows the SRFs corresponding to the middle and edge of the field at 400 nm. The FWHM difference is $\sim$6%. Thus the design satisfies the spectral uniformity targets with sufficient margin to allow for fabrication toler-

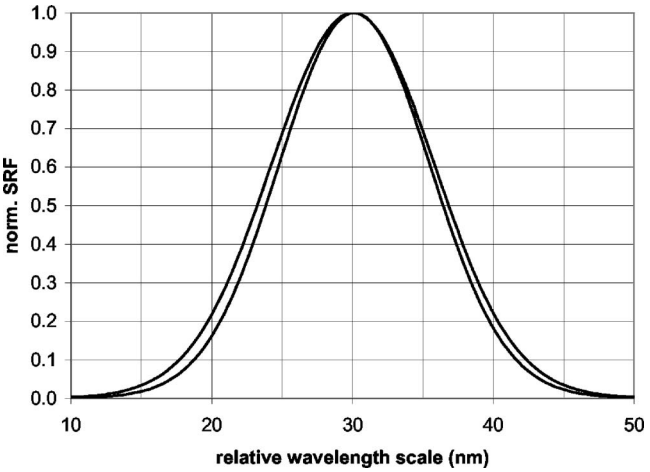

Fig. 9 Comparison of SRF at 3000 nm as predicted through the detailed diffraction propagation and the incoherent approximation, which neglects diffraction at the slit (wider curve). The predicted FWHM of 12.8 nm (narrow curve) is about 7% narrower.

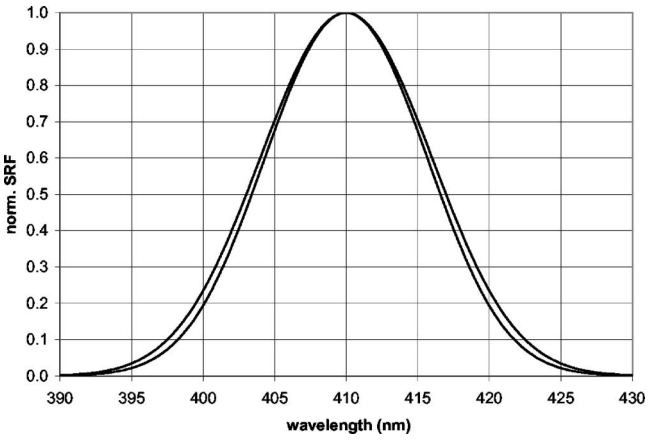

Fig. 10 Maximum predicted SRF nonuniformity for all wavelengths and fields (occurs at 400 nm, between fields 1 and 3 corresponding to the spot diagrams of Fig. 3). The broader curve is for the edge of the field. The FWHM varies between 13.1 and 14 nm, or ~6%.

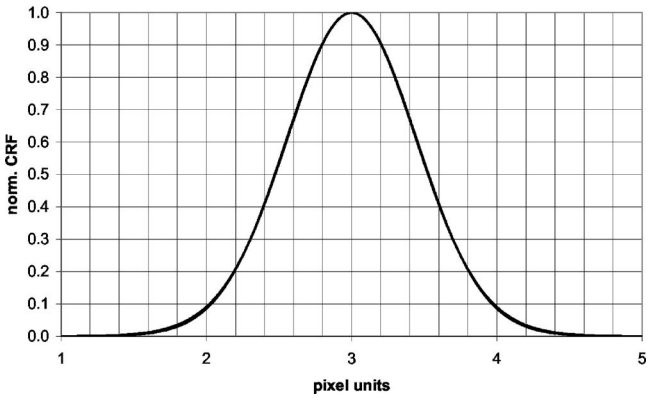

Fig. 11 CRF width nonuniformity based on an assumed 10% FWHM increase of the pixel response at the short wavelength. Two nearly coincident curves are shown, corresponding to the two extreme wavelengths (400 and 3000 nm). All field positions are similar. The FWHM is 1.05 to 1.06 pixel units.

ances. Computations for the as-toleranced system proceed along similar lines, but are not shown here. The results are summarized in Table 5.

5.3 *Assessment of Spatial Response and Spatial Uniformity*

In the cross-track (along the slit) direction, the slit has practically no effect and the complete system PSF must be taken into account. The spot centroids are used to assess geometric distortion (variation of magnification with wavelength). This is negligible at the design stage, but increases to 7% of a pixel after the assembly tolerances.

The CRF is the convolution of the cross-track system LSF with the detector pixel response. It can vary both with field and with wavelength. The CRF nonuniformity is assessed by selecting the field point at which its chromatic variation is maximum. However, inspection of the spot diagrams of Fig. 3 reveals that the spatial width of all PSFs is similar in the x direction, with most of the variation occurring along the spectral direction. This is an effect of the optimization procedure that produced deliberately degraded spots at the short wavelength end.

The residual variation of the cross-track LSF is balanced almost exactly by the assumed wavelength variation of the pixel response function with wavelength. Thus the predicted FWHM variation of the CRF is very small, as seen in Fig. 11. However, even if this balancing is not perfect, the residual variation is still expected to be small. Assembly and launch tolerances add equally small amounts to this type of nonuniformity (Table 5). This small variation would be expected to hold in the absence of atmospheric scattering.

The ARF is derived in two steps. First, a point source is scanned across the slit in the same manner as in the SRF computation. However, here the spectrometer acts as simply a light collector, although light diffracted outside the spectrometer aperture by the slit must also be considered at the long wavelengths. The resulting system transmittance represents the static form of the ARF, which is then further convolved with a rect function of width equal to the slit. This represents the effect of the integration time of the detector, assumed here to be equal to the instantaneous FOV (slit). The result of this convolution represents the expected ARF from orbit; it is shown in Fig. 12, which also shows the effect of neglecting diffraction from the slit.

Since only the telescope PSF can produce a smoothing of the ARF, we observe a nearly triangular response for the short wavelength where the telescope response is very sharp (there is little aberration and diffraction). At the longer wavelength, the Airy disk is larger and we observe a more Gaussian response. It can be seen that the difference in ARF between short and long wavelengths is rather small in terms of FWHM, but the comparison is somewhat problematic, since the curves do not have the same shape.

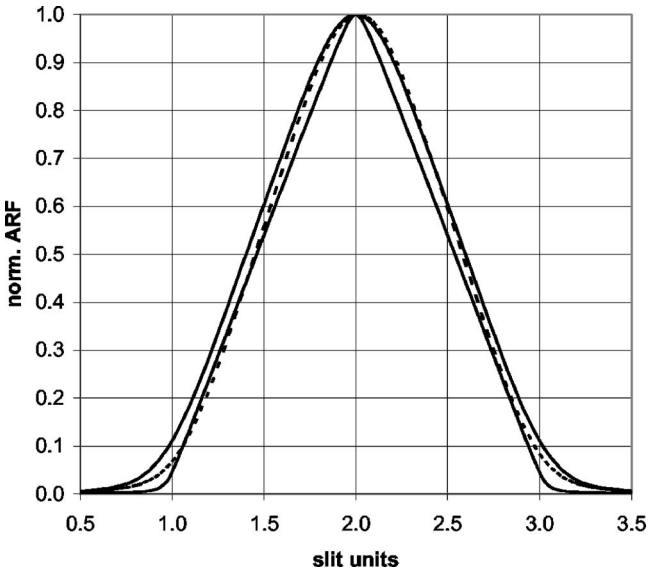

Fig. 12 Predicted ARF with motion blur. The narrow, almost triangular curve is for the 400-nm wavelength. The wider, solid curve is the incoherent approximation that results from neglecting diffraction losses inside the spectrometer at 3000 nm. The intermediate dashed curve is also for the long wavelength, but accounts properly for light diffracted from the slit and missing the spectrometer aperture. The FWHM varies between 1.07 and 1.12 slit (sample) units.

Small amounts of telescope defocus can in fact be somewhat beneficial in smoothing the chromatic variation of the ARF while having only a minimum impact on the CRF and none on the SRF. However, this line of reasoning is not pursued further here, because unknown factors such as the chromatic variation of the detector response may overwhelm these small theoretical improvements. The best balance between ARF and CRF can only be found in practice, once an instrument is in the state of assembly. Finally, assembly and launch tolerances have a small effect compared with the design nonuniformity (Table 5).

6 Conclusions

A compact and simple imaging spectrometer design is presented that achieves high uniformity of response, at the level of 10% of a pixel for both distortion and response function uniformity. This level of performance includes both assembly and launch tolerances, the latter assuming an appropriate level of control of thermal perturbations. The design achieves a broad response (400 to 3000 nm) and a wide field of view (24 deg). We demonstrate that a grating with constant response across its face may be preferable over a partitioned, multiblaze grating in terms of minimizing the variation of the spatial response. A bilinear groove design can provide an adjustable response that can be used in flattening the system SNR over a broad wavelength range. To our knowledge, this is the most compact and best performing system of its kind.

We also demonstrate the proper method of assessing the design quality in terms of parameters that relate directly to the instrument in-field performance, rather than typical optical design metrics. These parameters are the system spectral and spatial response functions and their variation with field and wavelength. We show that light diffracted outside the spectrometer aperture by the slit causes a measurable difference in the predicted response at the long wavelength end of this broad-band system, and we outline the method of computation that is necessary to account for this effect.

Acknowledgments

This research was performed at the Jet Propulsion Laboratory under a contract with the National Aeronautics and Space Administration. We thank Harold Sobel of JPL for setting up the SNR computational model.

References

1. R. N. Clark, G. A. Swayze, K. E. Livo, R. F. Kokaly, S. J. Sutley, J. B. Dalton, R. R. McDougal, and C. A. Gent, "Imaging spectroscopy: Earth and planetary remote sensing with the USGS Tetracorder and expert systems," *J. Geophys. Res., [Solid Earth]* **108**, (E12), 5131 (2003).
2. R. O. Green et al., "Imaging spectroscopy and the airborne visible/infrared imaging spectrometer (AVIRIS)," *Remote Sens. Environ.* **65**, 227–248 (1998).
3. J. S. Pearlman, P. S. Barry, C. C. Segal, J. Shepanski, D. Beiso, and S. L. Carman, "Hyperion, a space-based imaging spectrometer," *IEEE Trans. Geosci. Remote Sens.* **41**, 1160–1173 (2003)
4. E. A. Miller et al., "The visual and infrared mapping spectrometer for Cassini," *Proc. SPIE* **2803**, 206–220 (1996).
5. S. L. Murchie et al., "CRISM (compact reconnaissance imaging spectrometer for Mars) on MRO (Mars reconnaissance orbiter)," *Proc. SPIE* **5660**, 66–77 (2004).
6. R. O. Green, C. Pieters, P. Mouroulis, G. Sellar, M. Eastwood, S. Geier, and J. Shea, "The moon mineralogy mapper: Characteristics and early laboratory calibration results," presented at *Lunar and Planetary Science XXXVIII*, League City, TX, paper #2354 (2007).
7. P. Mouroulis, R. O. Green, and T. G. Chrien, "Design of pushbroom imaging spectrometers for optimum recovery of spectroscopic and spatial information," *Appl. Opt.* **39**, 2210–2220 (2000).
8. D. Kwo, G. Lawrence, and M. Chrisp, "Design of a grating spectrometer from a 1:1 Offner mirror system," *Proc. SPIE* **818**, 275–279 (1987)
9. P. Mouroulis, "Low-distortion imaging spectrometer designs utilizing convex gratings," *Proc. SPIE* **3482**, 594–601 (1998).
10. P. D. Maker, R. E. Muller, D. W. Wilson, and P. Mouroulis, "New convex grating types manufactured by electron beam lithography," *Diffract. Opt. Micro-opt.* **10**, 234–236 (1998).
11. P. Mouroulis, D. W. Wilson, P. D. Maker, and R. E. Muller, "Convex grating types for concentric imaging spectrometers," *Appl. Opt.* **37**, 7200–7208 (1998).
12. P. Mouroulis, J. J. Shea, and D. A. Thomas, "Design, tolerancing and alignment of pushbroom imaging spectrometers for high response uniformity," *Proc. SPIE* **4441**, 106–117 (2001).
13. K. D. Mielenz, "Spectroscope slit images in partially coherent light," *J. Opt. Soc. Am.* **57**, 66–74 (1967).
14. V. N. Mahajan, "Line of sight of an aberrated optical system," *J. Opt. Soc. Am. A* **2**, 833–846 (1985).

Pantazis Mouroulis is a graduate of the University of Athens (BSc in physics 1976) and the University of Reading (MSc and PhD in optics 1981). He is at present a senior research scientist and principal engineer at the Jet Propulsion Laboratory (JPL), where he supervises an optical technology group. His recent research interests focus on instrumentation for imaging spectroscopy.

R. Glenn Sellar has 18 years of experience in the design, integration, and testing of imaging spectrometers for ground-based, airborne, and spaceborne applications. He worked as an optical engineer on the Wind Imaging Interferometer (WINDII) for the Upper Atmosphere Research Satellite (UARS) and designed the optical system for the Fourier Transform HyperSpectral Imager (FTHSI) on MightySat II. He received a BEng degree in engineering physics from McMaster University in 1986, a MS degree in space sciences from the Florida Institute of Technology in 1993, and a PhD in optics from the University of Central Florida in 2003. He is a member of SPIE and is currently developing imaging spectrometers for planetary science and earth science applications at the Jet Propulsion Laboratory.

Daniel W. Wilson received the PhD in electrical engineering from the Georgia Institute of Technology in 1994. He is currently a principal engineer in the Microdevices Laboratory at Jet Propulsion Laboratory, California Institute of Technology. His research interests include the design, modeling, and electron-beam fabrication of diffractive optical components and instruments. Since joining JPL, he has contributed to the successful development of high-performance convex diffraction gratings, coronagraph occulting masks, transient-event imaging spectrometers, and particle velocity sensors.

James J. Shea received bachelor's degrees in physics and electrical engineering from the Worcester Polytechnic Institute, and masters degree in optical engineering from the University of Rochester. He has been with Swales Aerospace since 1993, which was recently acquired by Alliant Techsystems (ATK). Currently he is at the Pasadena California office, primarily supporting the Jet Propulsion Laboratory, where his activities have included optical design and analysis as well as optomechanical integration.

Robert O. Green is a senior research scientist at the Jet Propulsion Laboratory, where he has been performing research in imaging spectroscopy since 1983. He has been an experiment scientist for the Airborne Visible/Infrared Imaging Spectrometer (AVIRIS) since 1989. At present he is also co-investigator on the Mars Reconnaissance Orbiter CRISM imaging spectrometer, and co-investigator and instrument scientist for the NASA Discovery Mission Moon Mineral Mapper (M3). His research focuses on the end-to-end science requirements, from science question to calibration, to instrument, to photons. Recent research activities include spectroscopy of the three phases of water; atmospheric spectroscopy and radiative transfer; atmospheric correction; surface material identification and low concentration material abundance estimation.